ACS APPLIED MATERIALS & INTERFACES

www.acsami.org

Research Article

Enzyme-Free Electrochemical Biosensor Based on Localized DNA Cascade Displacement Reaction and Versatile DNA Nanosheets for Ultrasensitive Detection of Exosomal MicroRNA

Ping Liu,[⊥] Xiaoqing Qian,[⊥] Xinmin Li,[⊥] Lu Fan, Xinyu Li, Daxiang Cui, and Yurong Yan*

Cite This: *ACS Appl. Mater. Interfaces* 2020, 12, 45648−45656

Read Online

ACCESS | Metrics & More | Article Recommendations | Supporting Information

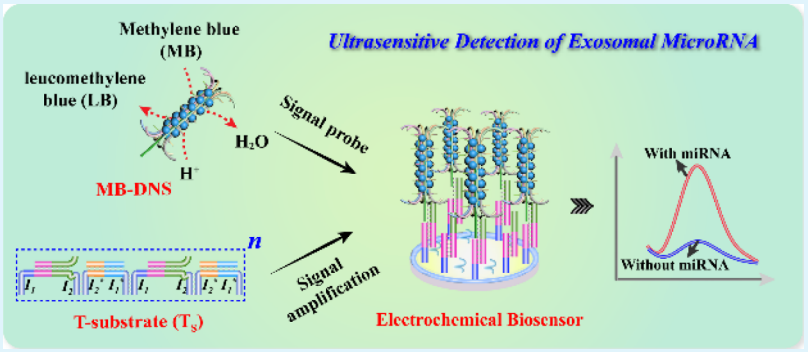

ABSTRACT: MicroRNA existing in exosomes (exo-miRNA) is a crucial and reliable biomarker for cancer screening and diagnosis. However, accurate detection of ultralow exo-miRNA amounts in real samples remains a challenge. Herein, a robust and ultrasensitive electrochemical biosensor was developed based on localized DNA cascade displacement reaction (L-DCDR) and versatile DNA nanosheets (DNSs) for enzyme-free analysis of exo-miRNA. The target activated L-DCDR repeatedly by consecutive toehold-mediated strand displacement, which released plentiful P strands to hybridize with capture probes immobilized on the electrode surface and DNS tags, generating an amplified electrochemical signal for the detection of exo-miRNA. The DNS could label-free load various electroactive molecules. The electrochemical biosensor revealed high sensitivity ranging from 0.1 fM to 1 nM with a limit of detection of 65 aM and good specificity. The constructed biosensor was demonstrated to be able to detect exo-miRNA derived from gastric cancer cell line (SGC-7901) and gastric cancer patients. In addition, the developed biosensor possessed several considerable advantages including simple substrate assembly, improved reaction rate, and high signal-to-noise ratio. Therefore, this strategy has great potential in bioanalysis and clinical diagnostics.

KEYWORDS: *electrochemical biosensor, exosomal microRNA, localized DNA circuit reaction, DNA nanostructure, enzyme-free*

INTRODUCTION

Exosomes are 30−200 nm extracellular vesicles which are released into peripheral circulation through fusion with the cell membrane.[1,2] Entrapping biologically active substances, such as miRNAs, proteins, and DNA, exosomes are endowed with function of cell-to-cell communication.[3,4] Studies have showed that exo-miRNAs are closely related to breast cancer, lung cancer, and gastric cancer.[5−7] In addition, exo-miRNAs are protected from RNase degradation by the exosomal membrane.[8] Hence, the analysis of exo-miRNAs provides great potential for early screening and accurate diagnosis of tumor. Currently, a common method for detection of exo-miRNAs is quantitative reverse transcription polymerase chain reaction (qRT-PCR).[9] However, this method suffers from laborious primer design, strict thermal cycle, and false positive, thus propelling researchers to develop new approaches with high accuracy for measurement of exo-miRNAs.[10−12]

In recent years, many novel methods have been developed for exo-miRNA detection,[13,14] for instance, molecular beacons and nucleic acid-functionalized gold nanoparticles revealing low sensitivity,[15,16] enzyme-assisted signal amplification strategies requiring strict reaction conditions,[17,18] and inorganic nanomaterials facing the challenge of controlling the size and shape of materials.[19,20] Accordingly, enzyme-free strategies using toehold-mediated DNA strand displacement as the core have been also explored due to low cost, high specificity, and simple operation.[21,22] Generally, the reaction

Received: August 13, 2020
Accepted: September 11, 2020
Published: September 11, 2020

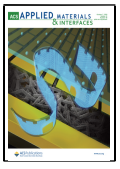

https://dx.doi.org/10.1021/acsami.0c14621
ACS Appl. Mater. Interfaces 2020, 12, 45648−45656

Scheme 1. Schematic Illustration of the Electrochemical Biosensor for Ultrasensitive Detection of Exo-miRNA; (A) Assembly Procedure of the MB-DNS; (B) the Operation Steps of the L-DCDR; (C) the Binding of the MB-DNS on the Electrode

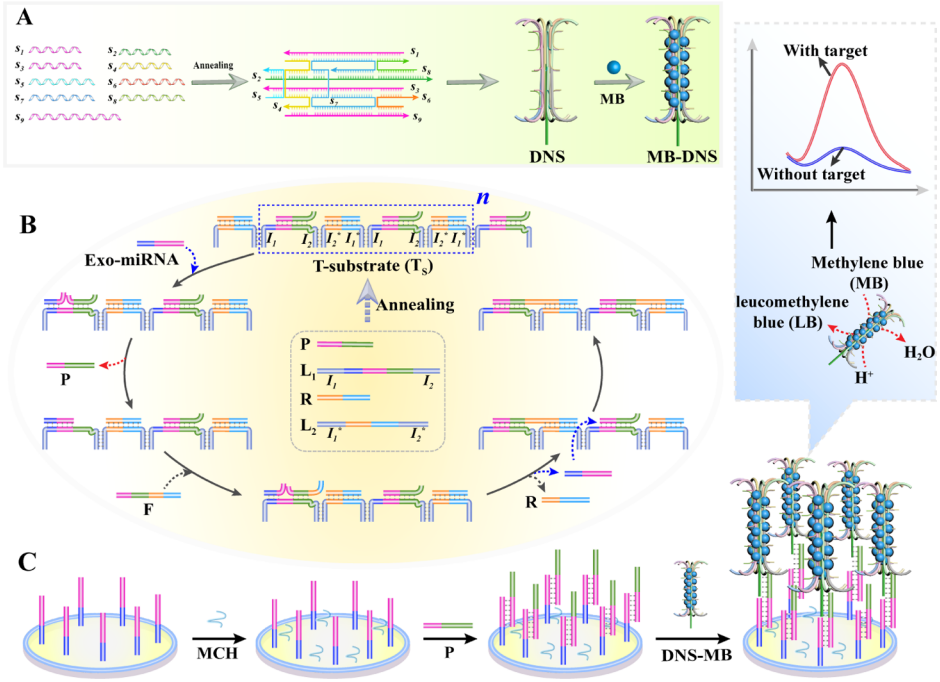

efficiency of these strategies are greatly compromised, resulting from the random collision and interaction of diffusible DNA reactants.

To improve local concentration and accelerate reaction, diffusible DNA reactants are regularly assembled in a compact space.[23] For example, Ju et al. designed a localized hybridization chain reaction (HCR) in which hairpin probes alternately bound to long DNA strands are produced by rolling circle amplification for mRNA detection.[24] Similarly, Wei et al. developed a localized catalytic hairpin assembly (CHA) for miRNA imaging in which CHA reactants were tethered to a DNA nanowire assembled through the hybridization of multiple single strands.[25] Although the localized substrates enhance the reaction speed, these strategies have at least one of the following defects: (i) the construction of localized substrates needs multiple assembly steps, leading to time- and labor-consuming; (ii) the intrinsic characteristics of CHA and HCR (unacceptable circuit leakage and strict reaction conditions that Mg^{2+} always have adverse repercussions on analytic performance) limit their clinical applications; and[26] (iii) the leakage which can be worse for the increased number of DNA hairpins in a compact space that are more prone to nonspecific interaction.[27]

Structural DNA nanotechnology has provided diverse amplified signal tags through simple DNA self-assembly and chemical modification for biosensing, such as horseradish peroxidase-labeled tetrahedron, streptavidin-conjugated dendrimer, and nanospheres.[28−30] Cross-linking through Watson−Crick base-pairing endows these tags robust stability in complex body liquid.[31] Moreover, the high addressability and precise controllability enable DNA-based nanostructures to anchor signal molecules with user-defined modes.[32] Particularly, sheetlike nanostructures possess large surface areas, offering lots of binding sites for signal molecules.[33] Taken together, we speculate that the DNA nanosheet (DNS) might be a promising material as a versatile and amplified signal tag by easily imbedding electroactive substances.

To bypass the disadvantages of localized reactions and further improve the sensitivity of the electrochemical biosensor, a robust and ultrasensitive biosensing strategy was developed for enzyme-free exo-miRNA detection based on localized DNA cascade displacement reaction (L-DCDR) and versatile DNS tags. First, the T-substrate (Ts) was assembled just by simple one-step annealing process to ensure sufficient hybridization of multiple short single strands. After adding exo-miRNA, the L-DCDR was quickly triggered, leading to the production of plentiful P strands. Then, the released P strands bound specifically to capture probes (CPs) and DNS tags, which generated an amplified electrochemical signal for the detection of exo-miRNA. In addition, the versatility of the DNS was demonstrated by label-free loading electroactive molecules, such as methylene blue (MB), doxorubicin (Dox), and G-quadruplex/hemin DNAzyme.

EXPERIMENTAL SECTION

Materials and Reagents. 6-Mercapto-1-hexanol (MCH) was obtained from Sigma-Aldrich (St Louis, MO, USA). 20 bp DNA Ladder was from TaKaRa Biotech (Dalian, China). Gold View was purchased from SBS Genetech (Beijing, China). The oligonucleotides purified by high-performance liquid chromatography from Sangon Biotech (Shanghai, China) are displayed in Table S1. All synthetic oligonucleotides were dissolved in Tris−ethylenediaminetetraacetic acid buffer (pH 8.0) and stored at −20 °C. Human normal gastric mucosal cell line (GES-1) and human gastric adenocarcinoma cell line (SGC-7901) were purchased from American Type Culture Collection (ATCC, Manassas, VA, USA). Fetal bovine serum, Dulbecco's modified Eagle medium, and penicillin−streptomycin were purchased from Hyclone. TRIzol was purchased from Beyotime Biotechnology. The hybridization buffer (pH 7.4) contained 10 mM Tris, 480 mM NaCl, and 5 mM $MgCl_2$. Tris−HCl buffer (pH 7.4) contained 0.02 M Tris, 0.1 M NaCl, and 0.5×10^{-2} M $MgCl_2$. Deionized water obtained from Millipore water purification system (≥18.2 Ω) was utilized in all tests, and other reagents were of analytical grade.

https://dx.doi.org/10.1021/acsami.0c14621
ACS Appl. Mater. Interfaces 2020, 12, 45648−45656

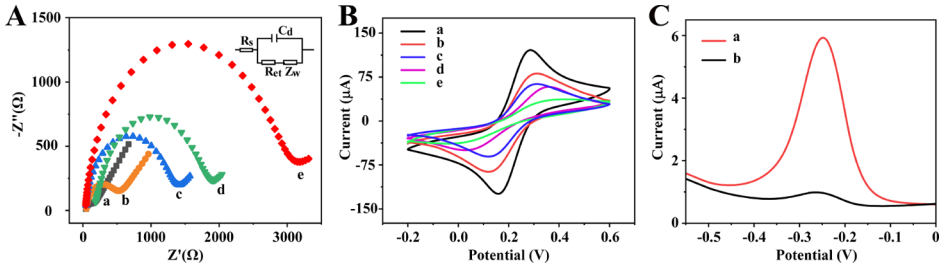

Figure 1. Feasibility of the biosensor. (A) EIS and (B) CV of different modified electrodes in 5×10^{-3} M $[Fe(CN)_6]^{3-/4-}$ containing 0.4 M KCl at (a) GE, (b) CP/GE, (c) MCH/CP/GE, (d) P/CP/MCH/GE, and (e) DNS/P/MCH/CP/GE. (C) DPV curves responding to (a) target and (b) blank control. [target] = 1 nM. [DNS] = 1 μM. Inset shows the equivalent circuit of the EIS: the solution resistance (R_s), the double layer capacitance (C_d), the charge-transfer resistance (R_{ct}), and the Warburg impedance (diffusion) element (Z_w).

Instruments. The biology transmission electron microscopy (TEM, Tecnai G2 Spirit Biotwin, JEOL Ltd.) was applied to characterize the typical morphologies of exosomes. Nanoparticle tracking analysis (NTA) was performed on a NanoSight NS300 instrument (Malvern Panalytical Ltd., Malvern, UK) to quantify exosomes. Electrochemical measurements were conducted by CHI660E electrochemical workstation (Shanghai Chenhua Instruments Co., Ltd., China) with a classical three-electrode system that consists of a platinum wire as the auxiliary electrode, an Ag/AgCl electrode as the reference electrode, and a 3 mm diameter gold electrode (GE) as the working electrode. An atomic force microscope (AFM) Dimension Icon (Bruker AXS, Germany) was utilized to characterize the size and morphology of the DNS.

Assembly of Reaction Substrates. All reaction substrates were annealed from 95 to 20 °C at a constant rate over 4 h in the hybridization buffer. The Ts contained 10 μM of R strands, P strands, L1 strands, and L2 strands. The DNS, containing 1 μM of DNA strands (S1−S9), was designed and constructed based on previous reports with some modifications.[34] The PRL_0 complex consisted of 10 μM of R strands, P strands, and L_0 strands. 100 μL of the DNS solution was mixed with 100 μL of 1 mM MB or DOX with slight shaking at 37 °C for 1 h to load MB or DOX. 100 μL of double-stranded DNA (dsDNA) assembled by S2 and S2* was mixed with 100 μL of MB (1 mM) to form MB-dsDNA. The assembly method of the DNAzyme-DNS comprising 1 μM of DNA strands (S1, S2, S3−G4, and S4−S9) was same with that of the DNS. The obtained Ts, DNS, MB-DNS, DOX-DNS, DNAzyme-DNS, MB-dsDNA, and PRL_0 complex were stored at 4 °C for further use.

Electrochemical Measurements. Different concentrations of exo-miRNA were added into the mixture of the Ts (0.5 μM) and F (0.5 μM) to trigger L-DCDR, followed by incubation at 37 °C for 1 h. Then, 8 μL of the mixture was dropped on the prepared electrodes (MCH/CP/GE) and reacted at 37 °C for 30 min. After washed with Tris−HCl buffer, the electrodes were loaded with 1 μM electrochemical indictors (MB-DNS, DOX-DNS, or DNAzyme-DNS) and incubated for 30 min. After the electrodes were washed again, the electrochemical measurements were performed with differential pulse voltammetry (DPV) in PBS. DPV measurement conditions were as follows: scanning potentials range from −0.5 to 0 V, a potential step of 5 mV, a pulse amplitude of 50 mV, a pulse width of 50 ms, and a pulse period of 200 ms. The DOX-DNS and DNAzyme-DNS tags were dropped on the electrode for 30 min with the scanning potentials range from −0.8 to −0.4 and −0.8 to −0.5 V, respectively.

Analysis of Exo-miRNA Derived from Human Serum Samples. The serum samples including healthy volunteer and gastric cancer patients were gained from Renji Hospital, School of Medicine, Shanghai JiaoTong University. For recovery experiments, the healthy serum samples were diluted to 10% in hybridization buffer. The detection steps of target miRNA followed that in buffer solution. In qRT-PCR analysis, U6 snRNA was used as an internal control.

The experimental detail of cell culture, exosomes isolation, and RNA extraction, characterization of exosomes, modification of the GE, and native polyacrylamide gel electrophoresis (PAGE) were depicted in Supporting Information.

RESULTS AND DISCUSSION

Design Principle of the Electrochemical Biosensor. Scheme 1 illustrates the principle of the electrochemical biosensor. Exo-miRNA-21 is highly enriched in tumor exosomes and can be utilized for the detection of gastric cancer.[35] Therefore, exo-miRNA-21 is chosen as the target. The DNS includes nine DNA strands (S1−S9), among which the crossover hybridizations form the sheetlike DNA nanostructure. The free part of the S2 chain in the DNS is used to hybridize with P strand. The DNS as a nanocarrier can label-free load electroactive MB, forming the MB-DNS (Scheme 1A). The L-DCDR is composed of Ts and F strands (Scheme 1B). The Ts is assembled by one-pot thermal annealing of P strand, R strand, L1 strand, and L2 strand. The L1 strand consists of blue region as toehold 1 (T1), green region as toehold 2 (T2) that is locked by P strand, and sequences I1 and I2 which are used to hybridize with I1* and I2* located in L2 strand, respectively. With the addition of the target, the target binds to the T1 and replaces the P strand by toehold-mediated strand displacement to expose the prelock T2. Subsequently, the F strand hybridizes with the exposed T2, displacing the target and the R strand with the extension of base pairing. Then, the displaced target binds fast to an adjacent T1 to trigger next circuit reaction, thus leading to the replacement of plentiful P strands. The displaced P strands hybridize with CPs immobilized on the electrode surface and further capture the MB-DNS (Scheme 1C). Serving as the electroactive indicator, the MB-DNS turns to leucomethylene blue after oxidization, and amplified electrochemical signals are obtained for the detection of exo-miRNA.

Feasibility of the Biosensing Strategy. The feasibility of the strategy was verified by electrochemical impedance spectra (EIS), cyclic voltammetry (CV), and DPV. First, the stepwise modified process of the bare GE was characterized by EIS and CV in the solution containing $[Fe(CN)_6]^{3-/4-}$. In EIS, the curve with a semicircular diameter was equal to the electron transfer resistance (R_{et}). As shown in Figure 1A, the bare GE showed an almost straight line (curve a), indicating the excellent electron transfer ability. The successful immobilization of CPs onto the bare electrode led to the increase of R_{et} (curve b). Subsequently, the assembly of MCH further triggered the R_{et} increase (curve c) because CPs and MCH hindered the electron transport from the solution to the electrode surface. After the mixture of exo-miRNA, Ts, and F strands was incubated on the electrode surface, the increase of R_{et} was observed (curve d), demonstrating the P strands released by target-mediated L-DCDR successfully bound to the CP. When the DNS was added to the above electrode, the R_{et}

https://dx.doi.org/10.1021/acsami.0c14621
ACS Appl. Mater. Interfaces 2020, 12, 45648−45656

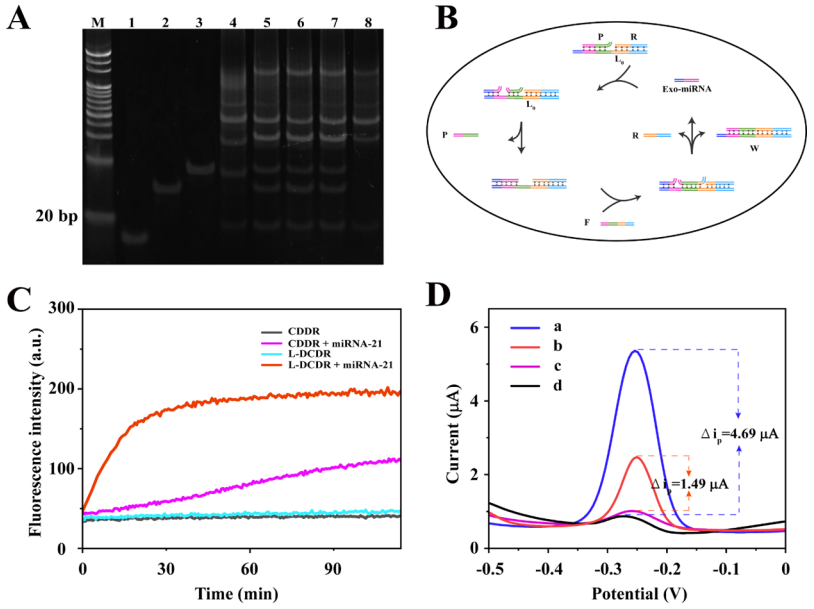

Figure 2. (A) Characterization of L-DCDR via PAGE. Lane 1: target, lane 2: P, lane 3: F, lane 4: the mixture of Ts and F, lanes 5−7: the mixture of Ts, F and various concentration of target, and lane 8: Ts. The concentrations of sequences were all 1 μM, except targets used in lane 5, 6, and 7 were 10, 50, and 100 nM, respectively. (B) Schematic of the CDDR. (C) Time-dependent fluorescence spectra of L-DCDR and CDDR responding to 10 nM target. (D) The DPV curves of L-DCDR and CDDR responding to (a) Ts + F + target, (b) PRL_0 + F + target, (c) PRL_0 + F, and (d) Ts + F. The concentrations of Ts, F, and PRL_0 were 0.5 μM. [target] = 100 pM.

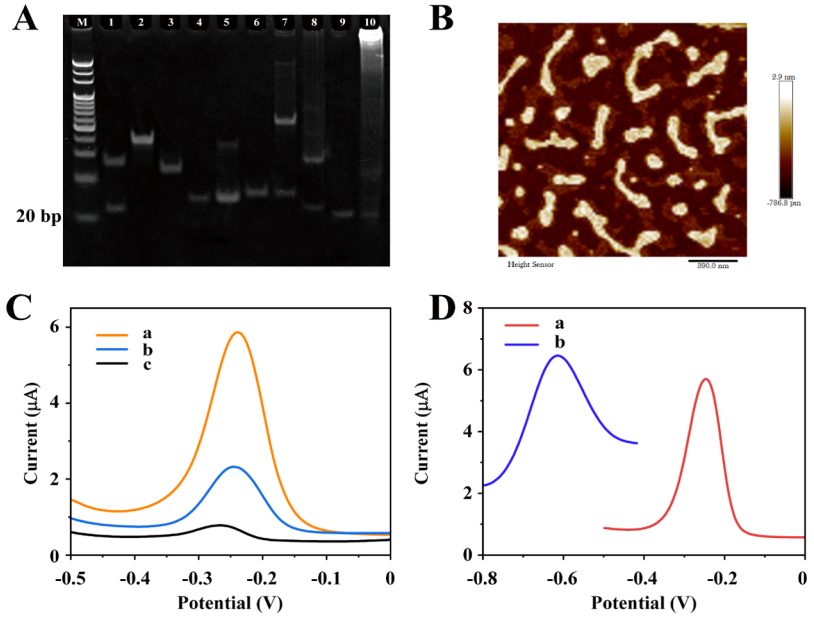

Figure 3. (A) Characterization of the DNS via PAGE. Lane M: DNA marker, lane 1−9: S1−S9 strands, and lane 10: the formed DNS. (B) Characterization of the DNS with AFM. Scale bar, 390 nm. (C) Verification of the larger surface area of the DNS. DPV curves responding to (a) MB-DNS, (b) MB-dsDNA, and (c) blank control. (D) Verification of the versatility of the DNS. DPV curves responding to (a) MB-DNS and (b) DOX-DNS. The concentrations of the MB-dsDNA, MB-DNS, and DOX-DNS were 1 μM. [target] = 1 nM.

increased sharply (curve e), proving the successful assembly of the DNS on the surface of the modified electrode by the part hybridization of the P strand and DNS, forming the DNS/P/CP three-decker complex. Figure 1B shows that the CV results at different stages were in good agreement with those measured by EIS. As shown in Figure 1C, the strong DPV signal could be detected in the presence of exo-miRNA, while there was no obvious signal in the blank control. According to these results, the developed electrochemical biosensor was available.

Characterization of the L-DCDR. The PAGE experiment was used to confirm the L-DCDR. As shown in Figure 2A, lanes 1, 2, 3, and 8 corresponded to target, P strand, F strand, and Ts complexes, respectively. In the absence of target, almost no P strand produced (lane 4), indicating that the constructed L-DCDR had ignorable background leak. In the presence of various concentrations of target, the F strands reduced while the plenty of P strands appeared (lane 5, 6 and 7), which proved that L-DCDR operated successfully. To further prove the superiority of L-DCDR, the conventional DNA displace-

https://dx.doi.org/10.1021/acsami.0c14621
ACS Appl. Mater. Interfaces 2020, 12, 45648−45656

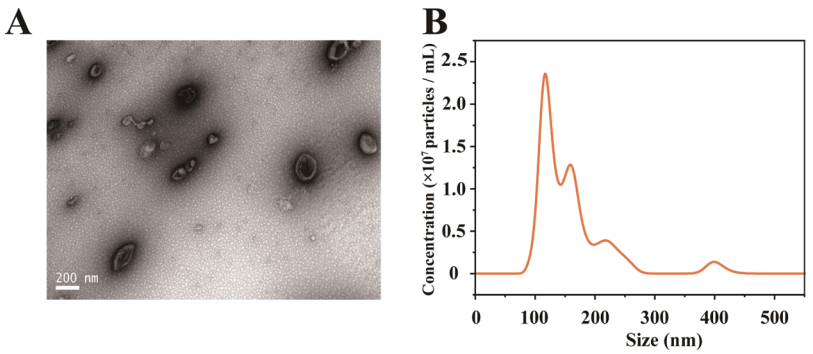

Figure 4. Characterization of isolated exosomes from SGC-7901 cells. (A) TEM image of exosomes. Scale bar, 200 nm. (B) NTA measuring size distribution of exosomes.

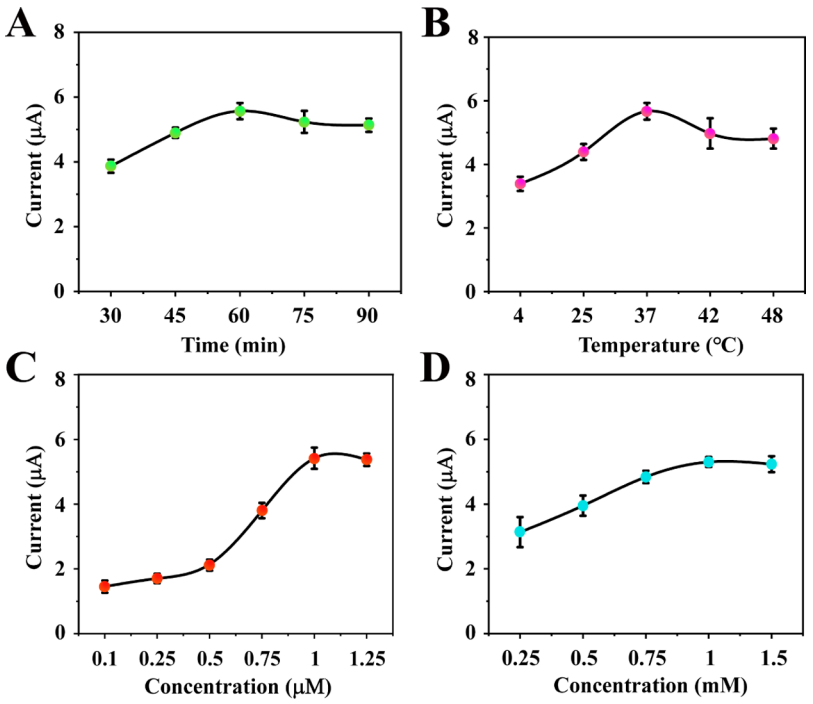

Figure 5. Optimizations of experimental parameters. Effects of (A) reaction time and (B) temperature of the L-DCDR and concentrations of (C) MB-DNS and (D) MB on the electrochemical signal. [target] = 1 nM. All results expressed as mean ± standard variation (n = 3).

ment reaction (CDDR, Figure 2B)[36] and L-DCDR were compared. First, the time-dependent fluorescence analysis was performed. The fluorescence recovery from the released FAM-labeled P strand that was quenched initially by BHQ-labeled R strands was measured. As shown in Figure 2C, compared with CDDR, the L-DCDR had faster fluorescence enhancement in response to the same concentration of target. However, the fluorescence signal produced by both strategies was hardly detected in the absence of target. The completion time for L-DCDR was around 3 times shorter than that of CDDR, and the fluorescence signal of L-DCDR was about 1.73 times higher than that of CDDR. Then, the DPV signals of L-DCDR and CDDR were also recorded. As shown in Figure 2D, in the absence of the target, the two strategies did not produce P chains, thus obtaining negligible current responses (curve c and d). This result indicated the constructed L-DCDR strategy had ignorable background leak even though diffusible DNA reactants were assembled in a compact space. However, in the presence of target, the obtained DPV signal of the L-DCDR (curve a) was significantly stronger than that of the CDDR (curve b), which demonstrated the L-DCDR possessed rapid reaction kinetics. Compared to the CDDR, the signal-to-noise ratio of the L-DCDR increased to 15 in the same reaction time. Thus, the L-DCDR possessed accelerated reaction, leading to short incubation time and improved the sensitivity. Although the random collision between F strand and Ts still existed in the L-DCDR, the target could move in the localized Ts with the help of the F strand after the first combination with Ts. The enhanced reaction rate and low background leakage of the developed L-DCDR were attributed to the following reasons: (1) two bulged thymidines located in the terminal of the Ts promoted the stability of the structure and boosted the speed of strand displacement reaction.[37,38] (2) Maintaining high concentrations of reactants in a compact space improved target transportation.[39,40]

Characterization of the DNS. The self-assembly of the DNS was verified by PAGE. As shown in Figure 3A, the migration speed of single DNA strands (S1−S9) was faster than that of the DNS (lane 10), which confirmed the successful assembly of the DNS. For further characterizing

https://dx.doi.org/10.1021/acsami.0c14621
ACS Appl. Mater. Interfaces 2020, 12, 45648−45656

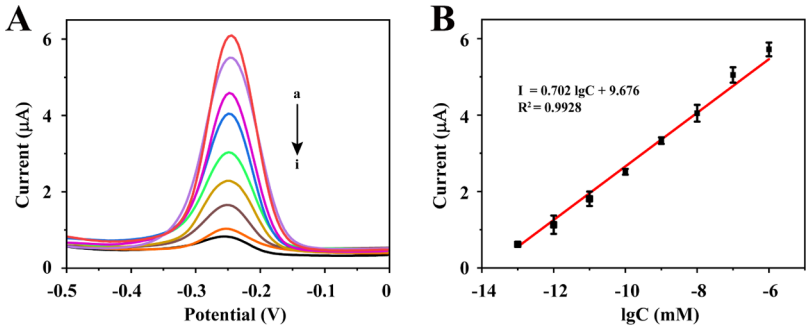

Figure 6. Evaluation of the sensitivity of the biosensor. (A) DPV curves responding to 10^{-6}, 10^{-7}, 10^{-8}, 10^{-9}, 10^{-10}, 10^{-11}, 10^{-12}, 10^{-13}, and 0 mM of target [from (a−i)]. (B) Linear correlation between the DPV peak and the logarithm of target concentrations ranging from 0.1 fM to 1 nM. All results are expressed as mean ± standard variation (n = 3).

the DNS, AFM was applied. As depicted in Figure 3B, the DNS possessed a typical sheetlike. The long rod-like nanostructures could be caused by the interaction between sheetlike structures. To prove the large surface area of the DNS, dsDNA embedded in MB (MB-dsDNA) was captured to the surface of electrode. As illustrated in Figure 3C, the generated signal of the MB-dsDNA was significantly smaller than that of the MB-DNS, indicating that the DNS provided more binding sites for signal molecules. The versatility of the DNS was further verified by label-free loading electroactive molecules such as MB, DOX, and DNAzyme. As shown in Figure 3D, MB-DNS (curve a), DOX-DNS (curve b), and DNAzyme-DNS (Figure S1) produced different electrochemical signals in corresponding potential. These results proved that the DNS was a versatile signal amplification indicator. In addition, the loading efficiency of the DNS toward MB was also evaluated by the UV−vis absorption spectrum. As depicted in Figure S2, MB had two typical absorption peaks at 680 and 300 nm, and the DNS showed a proper absorption peak at 260 nm, while the MB-DNS possessed three characteristic absorption peaks at 680, 300, and 260 nm, indicating the successful binding of MB to the DNS. By comparison of the difference in the absorption value of MB (0.78 a.u.) and the MB-DNS (0.6 a.u.) at 680 nm, the binding efficiency of the DNS toward MB was about 76.9%.

Characterization of Exosomes. To prove that miRNA was derived from exosomes, the collected exosomes were characterized by TEM and NTA first. As shown in Figure 4A, TEM showed that the collected exosomes had saucer-shape with sizes ranging from 30 to 200 nm, which were consistent with features of exosomes reported previously.[41] Subsequently, NTA was used to quantify exosomes and calculate average diameter of exosomes (Figure 4B). The concentration of the collected exosomes was about 1.73×10^{12} particles mL^{-1}, and the average size of the exosomes was approximately 112.6 nm. These experimental results showed that exosomes were successfully isolated.

Optimization of the Biosensor. Several experimental parameters, such as reaction time and temperature of the L-DCDR, concentrations of the MB-DNS and MB, and hybridization time of the P strand and CPs, were optimized to obtain the optimal analytical performance of the biosensor. For the biosensor, the higher electrochemical signal at the same concentration of target indicated the higher sensitivity. As shown in Figure 5A, the signal increased with the extension of reaction time and arrived to platform at 60 min, suggesting that L-DCDR was able to react adequately within 60 min. Thus, the optimum reaction time of the L-DCDR was 60 min. The reaction temperature of the L-DCDR from 4 to 48 °C was also evaluated (Figure 5B). The current signal experienced an upward trend from 4 to 37 °C. After that, the signal kept steady. Therefore, 37 °C was selected as the optimum reaction temperature of the L-DCDR. As depicted in Figure 5C, the signal grew with the augment of the MB-DNS concentration from 0.1 to 1 μM and reached a peak value at 1 μM. When more MB-DNSs were employed, the signal had not changed obviously, suggesting that the binding sites for MB-DNS reached saturation. Hence, the concentration of MB-DNS was fixed at 1 μM. As shown in Figure 5D, with the increase of concentration of MB, the current signal gradually improved and reached aa peak value at 1.0 mM. When the concentration of MB was greater than 1.0 mM, the signal did not change basically. Hence, 1.0 mM MB was optimal concentration. Figure S3A showed the change in the current signal with the incubation time of the P strand and CPs. The current intensity underwent an upward trend from 10 to 30 min and then kept stable. Therefore, 30 min was chosen as the optimal hybridization time of the P strand and CPs. Meanwhile, the immobilization concentration of CPs onto the electrode was also optimized. With the increase of CP concentration, the DPV response increased gradually to the maximum at 1 μM and then decreased (Figure S3B). Hence, the optimum concentration of CPs was 1 μM.

Sensitivity of the Biosensor. The sensitivity of the electrochemical sensor was determined under the optimal experimental conditions. As shown in Figure 6A, the results showed that DPV intensity increased gradually with the increase of miRNA-21 concentration from 0.1 fM to 1 nM. There was a good linear correlation between the DPV signal and the concentration of miRNA-21 (Figure 6B), fitted as $Y = 0.702 \lg C + 9.676$ ($R^2 = 0.9928$), where Y and C represented the DPV signal value and exo-miRNA-21 concentration, respectively. The limit of detection (LOD) was 65 aM based on the average signal of blank plus three times of the standard deviation.[42] Apart from exo-miRNA-21, it was in theory possible to achieve multiple detection of exo-miRNAs by only changing target-specific sequence. Compared to other biosensor for the detection of single exo-miRNA (Table S2) and multiple exo-miRNAs that needed to label many fluorophores (FAM, Cy3, and Cy5) and quenchers,[43−45] the label-free method had a lower or comparable LOD, which was ascribed to the integration of L-DCDR with MB-DNS.

Specificity, Reproducibility, and Stability of This Strategy. The DPV currents related to different types of

https://dx.doi.org/10.1021/acsami.0c14621
ACS Appl. Mater. Interfaces 2020, 12, 45648−45656

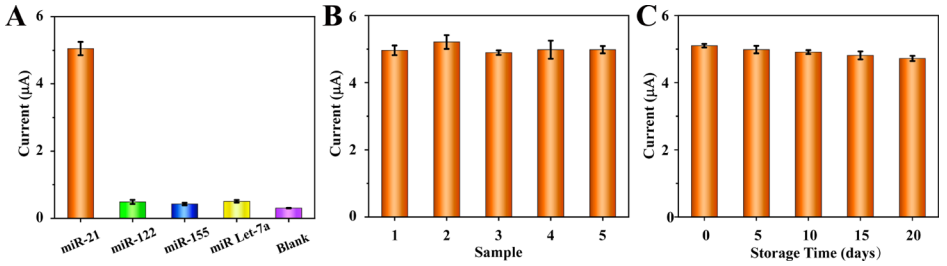

Figure 7. (A) Investigation of the specificity of the biosensor. Current signal responding to miRNA-21, miRNA-122, miRNA-155, miRNA Let-7a, and blank control. (B) Evaluation of the repeatability of the biosensor. The concentrations of all miRNAs were 100 pM. (C) Evaluation of the stability of the biosensor. All results are expressed as mean ± standard variation (n = 3).

miRNA, including miRNA-122, miRNA-155, and miRNA-let7a, were compared to evaluate the specificity of the developed biosensor. As shown in Figure 7A, the current responses from miRNA-122 (curve b), miRNA-155 (curve c), and miR-let-7a (curve d) were almost negligible. In contrast, high current intensity was obtained from the detection of miRNA-21, demonstrating the developed biosensor with high specificity. Moreover, the reproducibility of the biosensor was also investigated. The 100 pM miRNA-21 samples were assayed in five different batches. As seen in Figure 7B, the variable coefficient of the values was around 2.8%, indicating a good reproducibility of the developed electrochemical biosensor. The relevant DPV curves are shown in Figure S4. In addition, the stability of the biosensor was also evaluated. During 20 days, the electrochemical signal was measured at intervals of four days in the presence of 100 pM target. As shown in Figure 7C, the signal exhibited little fluctuation, even though the components of the biosensor were stored for 20 days at 4 °C. These results indicated that the developed electrochemical biosensor had good stability.

Real Sample Analysis. To demonstrate the potential application of the biosensor, Exo-miRNA-21 secreted from different cell lines were examined. As shown in Figure S5A, the current intensity produced by SGC-7901 cells obviously enhanced compared to GES-1 cells, indicating that the exo-miRNA-21 expression level of SGC-7901 cells significantly was higher than normal cells. On the other hand, exo-miRNA-21 derived from clinical samples was analyzed parallelly by our developed method and qRT-PCR. As shown in Figure S5B, the result of the proposed biosensor was in good agreement with that of qRT-PCR, and the level of exo-miRNA-21 from patients with gastric cancer distinctly improved compared to normal controls. To further evaluate the applicability of the biosensor, various known concentrations of miRNA-21 were spiked into diluted healthy human serum for carrying out recovery test. Table S3 shows that the recovery rates were between 99.8 and 107.1%, and the relative standard deviations ranged from 1.43 to 2.8%. These results demonstrated that the biosensor possessed high practicality and accuracy, which provided a potential analytical tool for clinical applications.

CONCLUSIONS

In summary, a robust and ultrasensitive electrochemical biosensor using L-DCDR and versatile DNS has been successfully developed for enzyme-free detection of exo-miRNA. The collaboration of L-DCDR and the DNS endowed the developed biosensor with rapid response and ultrahigh sensitivity. Compared to localized circuit reactions used previously, this developed electrochemical biosensor not only allowed L-DCDR substance to be assembled by the simple one-pot thermal annealing but also avoided exacerbation of nonspecific interaction. The sensing system only contained nucleic acids without the involvement of protein enzymes and inorganic nanomaterials, which achieved simple operation steps. In addition, as versatile electrochemical tags, DNS had the highly efficient loading capacity of MB, Dox, and DNAzyme. Compared with qRT-PCR, the electrochemical biosensor has advantages of enzyme-free, isothermal operation, simple probe design, and low-cost. Moreover, by performing exo-miRNA derived from tumor cells and clinical samples, the developed strategy has been demonstrated as a potentially tool for the early clinical diagnosis.

ASSOCIATED CONTENT

Supporting Information

The Supporting Information is available free of charge at https://pubs.acs.org/doi/10.1021/acsami.0c14621.

DNA sequences used in the work, cell culture, exosomes isolation and RNA extraction, characterization of exosomes, modification of the GE, PAGE, DPV curve of the DNAzyme-DNS, evaluation of the loading efficiency of the DNS toward MB by the UV−vis absorption spectrum, optimizations of hybridization time of the P strand and CPs and the concentration of CPs, DPV curves of investigation of the specificity and repeatability of the biosensor, comparison of the sensitivity of available methods for the detection of exo-miRNA, valuation of the practicability of the biosensor, and recovery test (PDF)

AUTHOR INFORMATION

Corresponding Author

Yurong Yan − *Key Laboratory of Clinical Laboratory Diagnostics (Ministry of Education), College of Laboratory Medicine, Chongqing Medical University, Chongqing 400016, China;* orcid.org/0000-0001-5910-6078; Email: yanyurong@cqmu.edu.cn

Authors

Ping Liu − *Key Laboratory of Clinical Laboratory Diagnostics (Ministry of Education), College of Laboratory Medicine, Chongqing Medical University, Chongqing 400016, China*

Xiaoqing Qian − *School of Biomedical Engineering, Shanghai Jiao Tong University, Shanghai 200240, China*

Xinmin Li − *Department of Laboratory Medicine, Chongqing Traditional Chinese Medicine Hospital, Chongqing 400016, China*

https://dx.doi.org/10.1021/acsami.0c14621
ACS Appl. Mater. Interfaces 2020, 12, 45648−45656

Lu Fan − *Key Laboratory of Clinical Laboratory Diagnostics (Ministry of Education), College of Laboratory Medicine, Chongqing Medical University, Chongqing 400016, China*
Xinyu Li − *Key Laboratory of Clinical Laboratory Diagnostics (Ministry of Education), College of Laboratory Medicine, Chongqing Medical University, Chongqing 400016, China*
Daxiang Cui − *Institute of Nano Biomedicine and Engineering, Department of Instrument Science and Engineering, Shanghai Engineering Center for Intelligent Diagnosis and Treatment Instrument National Center for Translational Medicine, Shanghai JiaoTong University, Shanghai 200240, China*

Complete contact information is available at: https://pubs.acs.org/10.1021/acsami.0c14621

Author Contributions

[⊥]P.L., X.Q., and X.L. contributed equally to this work.

Notes

The authors declare no competing financial interest.

■ ACKNOWLEDGMENTS

This work was funded by the financial support from the National Natural Science Foundation of China (81873980) and the Natural Science Foundation Project of Chongqing (cstc2018jcyjAX0349, cstc2018jcyjAX0132).

■ REFERENCES

(1) Kalluri, R.; LeBleu, V. S. The Biology, Function, and Biomedical Applications of Exosomes. *Science* **2020**, *367*, No. eaau6977.
(2) van Niel, G.; D'Angelo, G.; Raposo, G. Shedding Light on the Cell Biology of Extracellular Vesicles. *Nat. Rev. Mol. Cell Biol.* **2018**, *19*, 213−228.
(3) Mathieu, M.; Martin-Jaular, L.; Lavieu, G.; Théry, C. Specificities of Secretion and Uptake of Exosomes and Other Extracellular Vesicles for Cell-to-cell Communication. *Nat. Cell Biol.* **2019**, *21*, 9−17.
(4) Xu, R.; Rai, A.; Chen, M.; Suwakulsiri, W.; Greening, D. W.; Simpson, R. J. Extracellular Vesicles in Cancer - implications for Future Improvements in Cancer Care. *Nat. Rev. Clin. Oncol.* **2018**, *15*, 617−638.
(5) Lee, J. U.; Kim, W. H.; Lee, H. S.; Park, K. H.; Sim, S. J. Quantitative and Specific Detection of Exosomal MiRNAs for Accurate Diagnosis of Breast Cancer Using a Surface-Enhanced Raman Scattering Sensor Based on Plasmonic Head-Flocked Gold Nanopillars. *Small* **2019**, *15*, 1970091.
(6) Cazzoli, R.; Buttitta, F.; Di Nicola, M.; Malatesta, S.; Marchetti, A.; Rom, W. N.; Pass, H. I. MicroRNAs Derived from Circulating Exosomes as Noninvasive Biomarkers for Screening and Diagnosing Lung Cancer. *J. Thorac. Oncol.* **2013**, *8*, 1156−1162.
(7) Zheng, M.; Hou, L.; Ma, Y.; Zhou, L.; Wang, F.; Cheng, B.; Wang, W.; Lu, B.; Liu, P.; Lu, W.; Lu, Y. Exosomal Let-7d-3p and MiR-30d-5p as Diagnostic Biomarkers for Non-invasive Screening of Cervical Cancer and Its Precursors. *Mol. Cancer* **2019**, *18*, 76.
(8) Cheng, L.; Sharples, R. A.; Scicluna, B. J.; Hill, A. F. Exosomes Provide a Protective and Enriched Source of MiRNA for Biomarker Profiling Compared to Intracellular and Cell-Free Blood. *J. Extracell. Vesicles* **2014**, *3*, 23743.
(9) Alexander, M.; Hu, R.; Runtsch, M. C.; Kagele, D. A.; Mosbruger, T. L.; Tolmachova, T.; Seabra, M. C.; Round, J. L.; Ward, D. M.; O'Connell, R. M. Exosome-delivered MicroRNAs Modulate the Inflammatory Response to Endotoxin. *Nat. Commun.* **2015**, *6*, 7321.
(10) Chang, J.; Wang, X.; Wang, J.; Li, H.; Li, F. Nucleic Acid-Functionalized Metal-Organic Framework-Based Homogeneous Electrochemical Biosensor for Simultaneous Detection of Multiple Tumor Biomarkers. *Anal. Chem.* **2019**, *91*, 3604−3610.
(11) Gai, P.; Gu, C.; Hou, T.; Li, F. Integration of Biofuel Cell-Based Self-Powered Biosensing and Homogeneous Electrochemical Strategy for Ultrasensitive and Easy-To-Use Bioassays of MicroRNA. *ACS Appl. Mater. Interfaces* **2018**, *10*, 9325−9331.
(12) Gai, P.; Gu, C.; Li, H.; Sun, X.; Li, F. Ultrasensitive Ratiometric Homogeneous Electrochemical MicroRNA Biosensing via Target-Triggered Ru(III) Release and Redox Recycling. *Anal. Chem.* **2017**, *89*, 12293−12298.
(13) Liu, L.; Lu, H.; Shi, R.; Peng, X.-X.; Xiang, Q.; Wang, B.; Wan, Q.-Q.; Sun, Y.; Yang, F.; Zhang, G.-J. Synergy of Peptide-Nucleic Acid and Spherical Nucleic Acid Enabled Quantitative and Specific Detection of Tumor Exosomal MicroRNA. *Anal. Chem.* **2019**, *91*, 13198−13205.
(14) Lee, J.-H.; Choi, J.-H.; Chueng, S.-T. D.; Pongkulapa, T.; Yang, L.; Cho, H.-Y.; Choi, J.-W.; Lee, K.-B. Nondestructive Characterization of Stem Cell Neurogenesis by a Magneto-Plasmonic Nanomaterial-Based Exosomal MiRNA Detection. *ACS Nano* **2019**, *13*, 8793−8803.
(15) Zhai, L.-Y.; Li, M.-X.; Pan, W.-L.; Chen, Y.; Li, M.-M.; Pang, J.-X.; Zheng, L.; Chen, J.-X.; Duan, W.-J. In Situ Detection of Plasma Exosomal MicroRNA-1246 for Breast Cancer Diagnostics by a Au Nanoflare Probe. *ACS Appl. Mater. Interfaces* **2018**, *10*, 39478−39486.
(16) Gao, X.; Li, S.; Ding, F.; Fan, H.; Shi, L.; Zhu, L.; Li, J.; Feng, J.; Zhu, X.; Zhang, C. Rapid Detection of Exosomal MicroRNAs Using Virus-Mimicking Fusogenic Vesicles. *Angew. Chem., Int. Ed.* **2019**, *58*, 8719−8723.
(17) Wang, R.; Zhao, X.; Chen, X.; Qiu, X.; Qing, G.; Zhang, H.; Zhang, L.; Hu, X.; He, Z.; Zhong, D.; Wang, Y.; Luo, Y. Rolling Circular Amplification (RCA)-Assisted CRISPR/Cas9 Cleavage (RACE) for Highly Specific Detection of Multiple Extracellular Vesicle MicroRNAs. *Anal. Chem.* **2020**, *92*, 2176−2185.
(18) Bai, Z.; Gao, N.; Xu, H.; Wang, X.; Tan, L.; Pang, H.; Ma, H. Construction of an Ultra-sensitive Electrochemical Sensor Based on Polyoxometalates Decorated with CNTs and AuCo Nanoparticles for the Voltammetric Simultaneous Determination of Dopamine and Uric Acid. *Mikrochim. Acta* **2020**, *187*, 483.
(19) Xia, Y.; Wang, L.; Li, J.; Chen, X.; Lan, J.; Yan, A.; Lei, Y.; Yang, S.; Yang, H.; Chen, J. A Ratiometric Fluorescent Bioprobe Based on Carbon Dots and Acridone Derivate for Signal Amplification Detection Exosomal MicroRNA. *Anal. Chem.* **2018**, *90*, 8969−8976.
(20) Pang, Y.; Wang, C.; Lu, L.; Wang, C.; Sun, Z.; Xiao, R. Dual-SERS Biosensor for One-step Detection of MicroRNAs in Exosome and Residual Plasma of Blood Samples for Diagnosing Pancreatic Cancer. *Biosens. Bioelectron.* **2019**, *130*, 204−213.
(21) Wu, Q.; Wang, H.; Gong, K.; Shang, J.; Liu, X.; Wang, F. Construction of an Autonomous Nonlinear Hybridization Chain Reaction for Extracellular Vesicles-Associated MicroRNAs Discrimination. *Anal. Chem.* **2019**, *91*, 10172−10179.
(22) Guo, Q.; Yu, Y.; Zhang, H.; Cai, C.; Shen, Q. Electrochemical Sensing of Exosomal MicroRNA Based on Hybridization Chain Reaction Signal Amplification with Reduced False-Positive Signals. *Anal. Chem.* **2020**, *92*, 5302−5310.
(23) Liu, L.; Rong, Q.; Ke, G.; Zhang, M.; Li, J.; Li, Y.; Liu, Y.; Chen, M.; Zhang, X.-B. Efficient and Reliable MicroRNA Imaging in Living Cells via a FRET-Based Localized Hairpin-DNA Cascade Amplifier. *Anal. Chem.* **2019**, *91*, 3675−3680.
(24) Ren, K.; Xu, Y.; Liu, Y.; Yang, M.; Ju, H. A Responsive "Nano String Light" for Highly Efficient mRNA Imaging in Living Cells via Accelerated DNA Cascade Reaction. *ACS Nano* **2018**, *12*, 263−271.
(25) Wei, Q.; Huang, J.; Li, J.; Wang, J.; Yang, X.; Liu, J.; Wang, K. A DNA Nanowire Based Localized Catalytic Hairpin Assembly Reaction for MicroRNA Imaging in Live Cells. *Chem. Sci.* **2018**, *9*, 7802−7808.
(26) Jung, C.; Ellington, A. D. Diagnostic Applications of Nucleic Acid Circuits. *Acc. Chem. Res.* **2014**, *47*, 1825−1835.
(27) Sun, X.; Wei, B.; Guo, Y.; Xiao, S.; Li, X.; Yao, D.; Yin, X.; Liu, S.; Liang, H. A Scalable "Junction Substrate" to Engineer Robust DNA Circuits. *J. Am. Chem. Soc.* **2018**, *140*, 9979−9985.
(28) Li, M.; Wang, C.; Di, Z.; Li, H.; Zhang, J.; Xue, W.; Zhao, M.; Zhang, K.; Zhao, Y.; Li, L. Engineering Multifunctional DNA Hybrid Nanospheres Through Coordination-Driven Self-Assembly. *Angew. Chem., Int. Ed.* **2019**, *58*, 1350−1354.

(29) Liu, Q.; Ge, Z.; Mao, X.; Zhou, G.; Zou, X.; Shen, J.; Shi, J.; Li, J.; Wang, L. Valency-Controlled Framework Nucleic Acid Signal Amplifiers. *Angew. Chem., Int. Ed.* **2018**, *57*, 7131−7135.
(30) Zhao, Y.; Hu, S.; Wang, H.; Yu, K.; Guan, Y.; Liu, X.; Li, N.; Liu, F. DNA Dendrimer-Streptavidin Nanocomplex: An Efficient Signal Amplifier for Construction of Biosensing Platforms. *Anal. Chem.* **2017**, *89*, 6907−6914.
(31) Liu, Q.; Wang, D.; Yuan, M.; He, B. F.; Li, J.; Mao, C.; Wang, G. S.; Qian, H. Capturing Intracellular Oncogenic MicroRNAs With Self-Assembled DNA Nanostructures for MicroRNA-based Cancer Therapy. *Chem. Sci.* **2018**, *9*, 7562−7568.
(32) Liu, N.; Liedl, T. DNA-Assembled Advanced Plasmonic Architectures. *Chem. Rev.* **2018**, *118*, 3032−3053.
(33) Ge, J.; Zhao, Y.; Li, C.; Jie, G. Versatile Electrochemiluminescence and Electrochemical "On-Off" Assays of Methyltransferases and Aflatoxin B1 Based on a Novel Multifunctional DNA Nanotube. *Anal. Chem.* **2019**, *91*, 3546−3554.
(34) Zhou, C.; Yang, Z.; Liu, D. Reversible Regulation of Protein Binding Affinity by a DNA Machine. *J. Am. Chem. Soc.* **2012**, *134*, 1416−1418.
(35) Wang, M.; Yu, F.; Ding, H.; Wang, Y.; Li, P.; Wang, K. Emerging Function and Clinical Values of Exosomal MicroRNAs in Cancer. *Ther. Nucleic Acids* **2019**, *16*, 791−804.
(36) Zhang, D. Y.; Turberfield, A. J.; Yurke, B.; Winfree, E. Engineering Entropy-driven Reactions and Networks Catalyzed by DNA. *Science* **2007**, *318*, 1121−1125.
(37) Chen, X. Expanding the Rule Set of DNA Circuitry With Associative Toehold Activation. *J. Am. Chem. Soc.* **2012**, *134*, 263−271.
(38) Leontis, N. B.; Kwok, W.; Newman, J. S. Stability and Structure of Three-Way DNA Junctions Containing Unpaired Nucleotides. *Nucleic Acids Res.* **1991**, *19*, 759−766.
(39) Chatterjee, G.; Dalchau, N.; Muscat, R. A.; Phillips, A.; Seelig, G. A Spatially Localized Architecture for Fast and Modular DNA Computing. *Nat. Nanotechnol.* **2017**, *12*, 920.
(40) Bui, H.; Miao, V.; Garg, S.; Mokhtar, R.; Song, T.; Reif, J. Design and Analysis of Localized DNA Hybridization Chain Reactions. *Small* **2017**, *13*, 1602983.
(41) Huang, R.; He, L.; Xia, Y.; Xu, H.; Liu, C.; Xie, H.; Wang, S.; Peng, L.; Liu, Y.; Liu, Y.; He, N.; Li, Z. A Sensitive Aptasensor Based on a Hemin/G-Quadruplex-Assisted Signal Amplification Strategy for Electrochemical Detection of Gastric Cancer Exosomes. *Small* **2019**, *15*, 1900735.
(42) Jiang, J.; Lin, X.; Diao, G. Smart Combination of Cyclodextrin Polymer Host-Guest Recognition and Mg^{2+}-Assistant Cyclic Cleavage Reaction for Sensitive Electrochemical Assay of Nucleic Acids. *ACS Appl. Mater. Interfaces* **2017**, *9*, 36688−36694.
(43) Wang, H.; He, D.; Wan, K.; Sheng, X.; Cheng, H.; Huang, J.; Zhou, X.; He, X.; Wang, K. In Situ Multiplex Detection of Serum Exosomal MicroRNAs Using an All-in-one Biosensor for Breast Cancer Diagnosis. *Analyst* **2020**, *145*, 3289−3296.
(44) Chen, C.; Zong, S.; Wang, Z.; Lu, J.; Zhu, D.; Zhang, Y.; Zhang, R.; Cui, Y. Visualization and Intracellular Dynamic Tracking of Exosomes and Exosomal MiRNAs Using Single Molecule Localization Microscopy. *Nanoscale* **2018**, *10*, 5154−5162.
(45) Cho, S.; Yang, H. C.; Rhee, W. J. Simultaneous Multiplexed Detection of Exosomal MicroRNAs and Surface Proteins for Prostate Cancer Diagnosis. *Biosens. Bioelectron.* **2019**, *146*, 111749.

https://dx.doi.org/10.1021/acsami.0c14621
ACS Appl. Mater. Interfaces 2020, 12, 45648−45656